IJCRT.ORG ISSN : 2320-2882

INTERNATIONAL JOURNAL OF CREATIVE RESEARCH THOUGHTS (IJCRT)

An International Open Access, Peer-reviewed, Refereed Journal

Co_3NiBaO_6 Nanoparticles as Efficient Visible-Light Photocatalysts for Multifunctional Dye Degradation Applications

[1]Jinesh Menaria, [2]Dushyant Kumar Prajapati, [3]Jeevan Kunwar Chouhan, [4]Tejveer Singh Tanwer, [5]Shipra Bhardwaj

[1]Research scholar, [2]Research scholar, [3]Research scholar, [4]Research scholar, [5]Proffesor

Department of Chemistry, Government Meera Girls' College,

Mohan Lal Shukhadia University, Udaipur, Rajasthan, India

Abstract : Co_3NiBaO_6 nanoparticles were successfully synthesized via a co-precipitation method under optimized conditions. Their structural and morphological features were comprehensively characterized using XRD, XPS, FTIR, FE-SEM, and EDS analyses, with particular attention to the influence of calcination temperature on crystallinity and morphology. UV–Vis absorption spectra displayed a characteristic peak at 495–496 nm and optical bandgap of approximately 3.29 eV, which was further supported by photoluminescence (PL) studies. The photocatalytic activity of the synthesized nanoparticles was evaluated for the degradation of Toluidine Blue (TB), Reactive Red 35 (RR), and Eosin Yellow (EY) under visible light irradiation. Systematic kinetic studies revealed optimal degradation efficiencies of 80–89% within 40–70 minutes. Scavenger experiments identified hydroxyl radicals and photogenerated holes (h^+) as the predominant reactive species responsible for pollutant degradation into smaller, non-toxic intermediates. Moreover, the catalyst exhibited excellent reusability, retaining stable photocatalytic performance over four successive cycles. Based on these results, a plausible photocatalytic degradation mechanism has been proposed and discussed.

Keywords: Photocatalysis, Photodegradation, Coprecipitation, Dye Degradation, Water treatment.

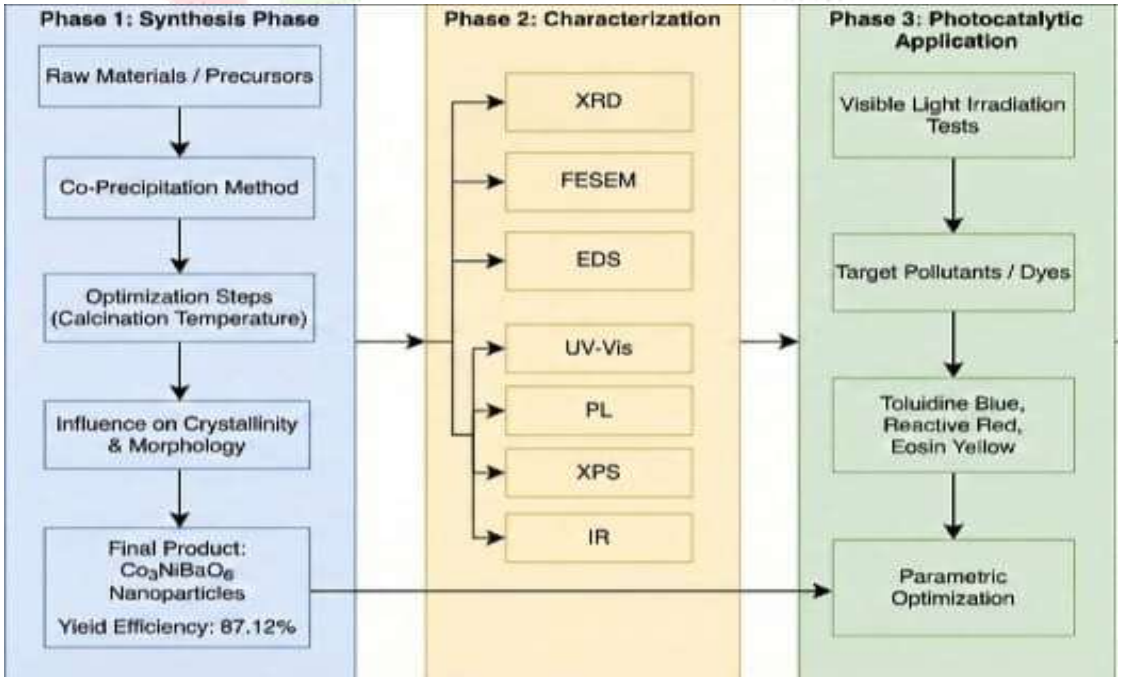

I. Introduction

Water pollution caused by synthetic dyes from textile industries represents a significant threat to both ecosystems and human health, as these effluents often contain highly stable and toxic organic pollutants. Conventional treatment methods, including adsorption and biological degradation, are generally ineffective due to the persistent and recalcitrant nature of these compounds. Consequently, advanced remediation strategies are required to achieve efficient degradation. Among these, photocatalysis—utilizing solar energy through semiconductor nanomaterials—has gained attention as a green and sustainable approach for the complete mineralization of dyes into environmentally benign products. Semiconductor metal oxides such as TiO_2 have been widely investigated for photocatalytic applications; however, their wide band gap restricts efficient utilization of visible light, thereby motivating research into novel mixed metal oxides with enhanced visible-light activity [1][2]. Cobalt-based oxide nanoparticles have received considerable attention in recent years due to their remarkable catalytic properties and diverse applications, particularly in environmental remediation. Notably, cobalt oxide (CoO) and cobalt sesquioxide (Co_2O_3) nanoparticles have shown promise in degrading various organic pollutants, including synthetic dyes prevalent in industrial effluents. Their unique electronic structures and high surface areas enable these nanoparticles to generate reactive oxygen species (ROS) upon light irradiation, which play a crucial role in the oxidative degradation of organic pollutants. Furthermore, the straightforward synthesis and adjustable physicochemical properties of cobalt oxide-based nanoparticles offer versatility and customization for specific applications in dye degradation [3]. Barium oxide nanoparticles feature high surface area and unique physicochemical properties ideal for catalytic degradation. These NPs excel in oxidative breakdown reactions, emerging as prime candidates for dye-laden wastewater remediation—their inherent catalysis converts organics to less harmful byproducts, curbing pollution and safeguarding health [4]. Nickel oxide nanoparticles deliver outstanding catalytic efficiency, broad surface area, and modifiable surface properties for aqueous organic dye degradation. Built-in photocatalytic traits spark and hasten illumination-based breakdown, offering eco-friendly, low-energy wastewater purification. Studies validate superior performance on azo, anthraquinone, and triarylmethane dyes at optimized settings [5]. Capitalizing on quaternary photocatalyst benefits in AOPs, this research unveils innovative Co_3NiBaO_6 synthesis, analysis, and Toluidine blue elimination from wastewater.

II. Experimental

Material and Method

Metal salt precursors were dissolved in distilled water to prepare 0.1 M aqueous solutions. Stoichiometric quantities of cobalt nitrate hexahydrate (14.52 g), nickel chloride hexahydrate (11.88 g), and barium nitrate (13.06 g) were used, with initial pH values of 6.1, 5.6, and 7.2, respectively. After filtration, the solutions were combined and magnetically stirred for 4 h at room temperature (25 °C) to obtain a clear mixture (pH 6.7). A 5 N NaOH solution was added dropwise under constant stirring until complete precipitation (pH 9.8). The precipitate was aged for 30 min, filtered, washed with distilled water to remove impurities, ground, and dried at 120 °C for 150 min, yielding 29.36 g of intermediate powder. Subsequent calcination at 500 °C for 4 h produced 25.58 g of dark black Co_3NiBaO_6 nanocomposite with a yield of 87.12%. For photocatalytic kinetics, aqueous dye solutions of Toluidine Blue, Eosin Yellow, and Reactive Red 35 were prepared, their pH measured, and the catalyst added. Under light irradiation, optical density (OD) was monitored over time, and a linear log (OD) vs time plot confirmed pseudo-first-order degradation behaviour (Figure 9).

Instumentation

Powder X-ray diffraction (XRD) patterns were obtained using a PANalytical X'Pert Pro diffractometer with Ni-filtered Cu Kα radiation (40 kV, 40 mA) and monochromatized Cu Kα (λ = 1.5418 Å), scanning 4°–80° in 2θ. Surface morphology, roughness, and elemental composition were analyzed via Nova Nano FE-SEM 450 (FEI) equipped with energy-dispersive X-ray spectroscopy. XPS spectra were recorded on a Physical Electronics PHI 5000 VersaProbe III instrument. UV-vis diffuse reflectance spectra were acquired using a PerkinElmer UV-vis NIR spectrophotometer. Photoluminescence (PL) data were obtained with a PerkinElmer FL 8500 fluorescence spectrophotometer (model FL85K21010402). FT-IR spectra of samples as KBr pellets were measured in the 400–4000 cm^{-1} range using a PerkinElmer Spectrum 2 spectrometer.

The absorbance of the dye was measured using a UV–Vis spectrophotometer (CHINO). Using the following formula, the degradation percentage of the dye was calculated:

$$\% \text{ degradation} = A_o - A_t / A_o \times 100$$

Where, A_o and A_t represent the initial absorbance and final absorbance of the dye at different time intervals, respectively.

III. Result and Discussion

3.1 Synthesis

Co_3NiBaO_6 nanocomposites were synthesized via co-precipitation using 0.1 M aqueous solutions of stoichiometric metal salts: cobalt nitrate hexahydrate (14.52 g, initial pH 6.1), nickel chloride hexahydrate (11.88 g, initial pH 5.6), and barium nitrate (13.06 g, initial pH 7.2). The filtered precursor solutions were magnetically stirred at 25°C for 4 hours to achieve a homogeneous mixture (pH 6.7). Precipitation was induced by dropwise addition of 5N NaOH under constant agitation until pH 9.8, followed by 30 minutes of coagulation stirring. The precipitate was collected via vacuum filtration, repeatedly washed with distilled water to remove impurities, pulverized using a mortar-pestle, and dried in a microwave oven at 120°C for 150 minutes (29.36 g intermediate yield). Final calcination at 500°C for 4 hours produced 25.58 g of dark black Co_3NiBaO_6 nanocomposite powder with 87.12% overall yield.

3.2 Element composition study

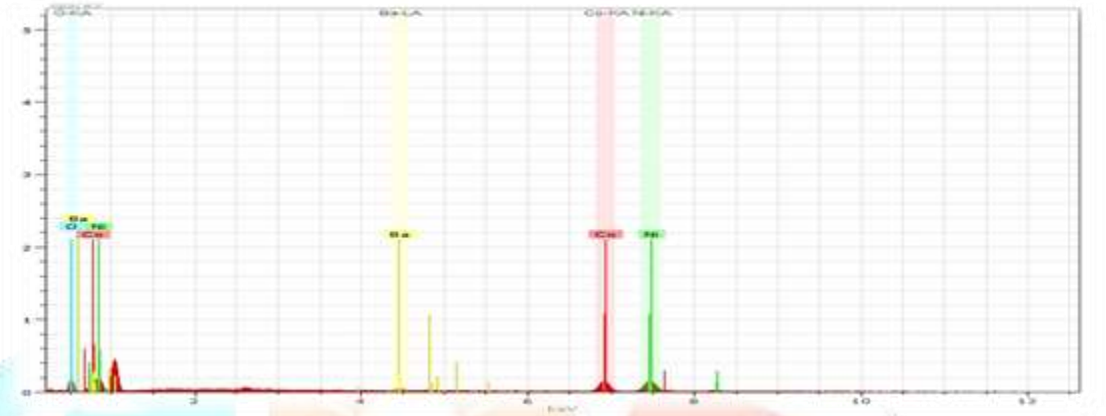

Figure 1: EDX Spectra with elemental mapping of Co_3NiBaO_6 nanoparticle

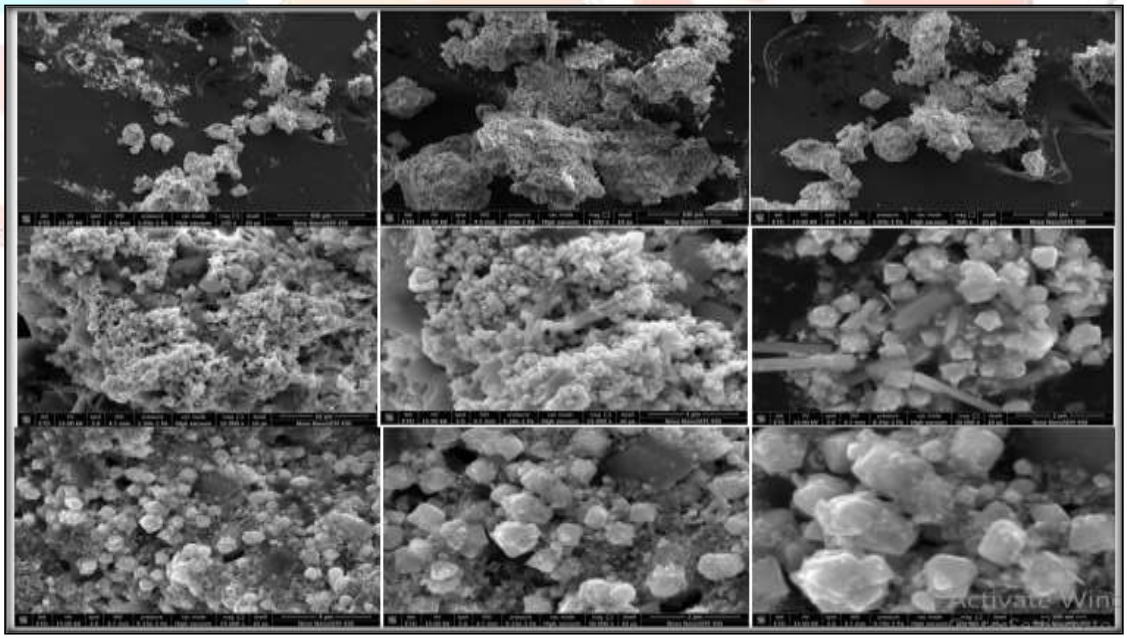

Figure 2: FESEM images of Co_3NiBaO_6 photocatalyst

EDX analysis of Co_3NiBaO_6 nanoparticles (figure 1) verifies stoichiometry with Co:Ni:Ba:O weight ratios of approx 3:1:1:6, confirming successful quaternary synthesis. FESEM images (figure 2) display spherical-cubic shapes with limited size distribution. Hierarchical structure included micron-scale clusters of highly agglomerated nanosized primary particles, featuring irregular aggregates, flake-like forms, rod/needle, and plate-like elements and Cluster surfaces exhibited high roughness, porosity, edges, and inter-particle voids from sintering, forming a sponge-like architecture. This boosts accessible surface area and reaction sites, aiding photocatalytic dye degradation efficiency.

3.3. Elemental ratio study:

XPS analysis (Figure 3) determined the chemical and electronic states of the synthesized material and the coordination environment of cobalt, nickel, and barium components. XPS spectra and deconvoluted individual-element plots are presented in Figures 2.7 and 2.8. Chemical composition and elemental constituents were examined, with focus on Co 2p, Ni $2p_{3/2}$, Ba $3d_{5/2}$, C1s, and O1s orbital transitions. Distinct XPS peaks at 780 eV and 795 eV for Co $2p_{3/2}$ indicated cobalt ions in +3 and +2 oxidation states [6] [7]. The spectrum revealed peaks at 780.1 eV and 795.72 eV corresponding to Ba $3d_{5/2}$, confirming barium as +2 oxidation state and BaO presence [8]. A distinct peak at 854 eV binding energy for Ni $2p_{3/2}$ confirmed nickel ions in +2 oxidation state, indicating NiO existence [6]. The O1s XPS spectrum exhibited a broad peak between 531.23-533.27 eV corresponding to oxygen vacancies and surface-adsorbed hydroxyl groups from ambient water exposure on the oxide [9]. This observation revealed the mixed metal oxide catalyst with surface oxygen vacancies is susceptible to ambient-air oxidation. High water adsorption energy makes such mixed metal oxide catalysts with surface oxygen vacancies vulnerable to oxidation under ambient conditions. This finding emphasizes water's high adsorption energy role in making mixed metal oxide materials or catalysts with surface oxygen vacancies vulnerable to oxidation during ambient exposure. Presence of Co^{2+}, Co^{3+}, Ni^{2+}, and Ba^{2+} ions in the synthesized sample is confirmed by the XPS spectra.

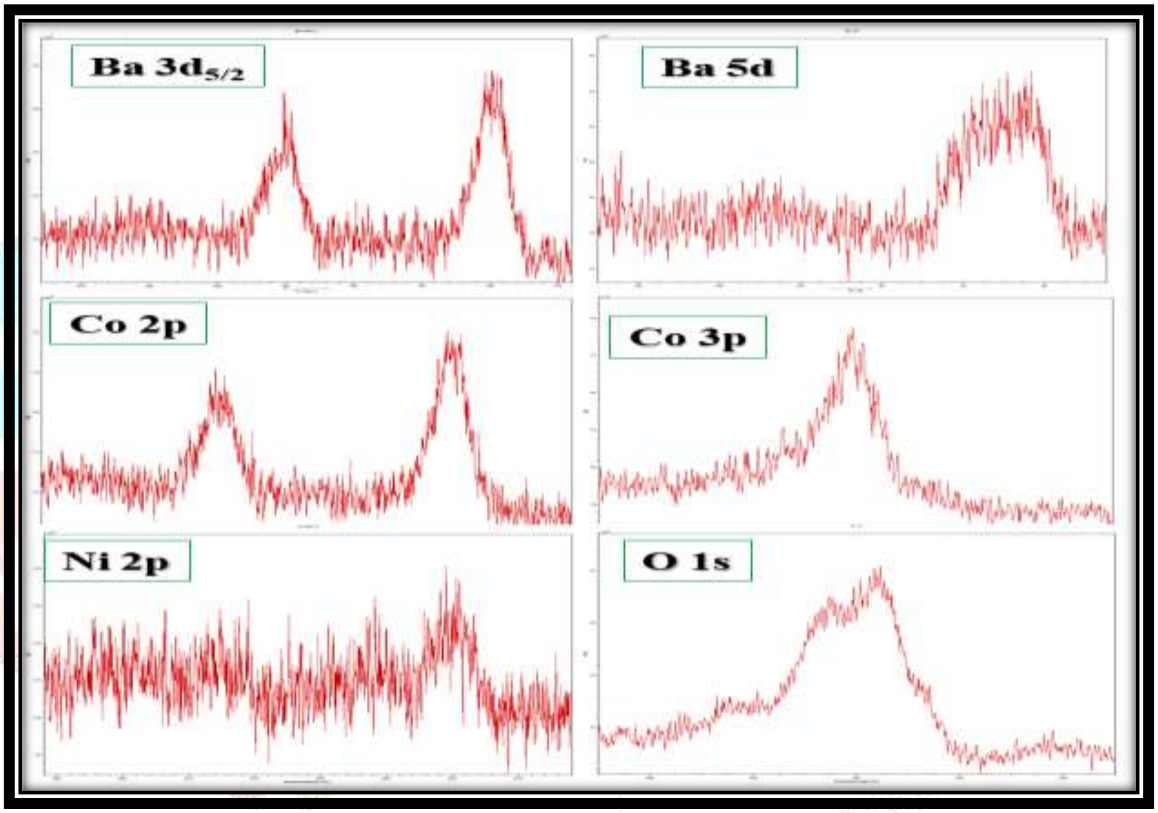

Figure 3: XPS spectra of individual elements

3.4. Crystal size calculation:

The crystal structure and phase purity of the synthesized Co_3BaNiO_6 nanomaterial were verified using powder X-ray diffraction analysis (Figure 4), with refined parameters listed in Table 1. The XRD pattern exhibited sharp, high-intensity peaks characteristic of excellent crystallinity. The primary peak at $2\theta \approx 31.98°$ ($d = 2.80$ Å), assigned to the (110) plane of hexagonal perovskite structure, matches Ba-Co-Ni solid solutions reported by Takeda in 1975 [10] and shows 100% relative intensity indicating preferred orientation for enhanced catalytic stability [11]. Supporting reflections at $2\theta = 20.34°$, 24.60°, 26.56°, 43.56°, and 45.70° correspond to (100), (101), (002), (201), and (202) planes, respectively, confirming the 2H-$BaCoO_3$-type hexagonal lattice described by Felser et al. in 1999 [12].

Average crystallite size (D) was determined via Debye-Scherrer equation: $D = K\lambda / (\beta \cos \theta)$ where $K = 0.9$, $\lambda = 0.15406$ nm (Cu Kα), β = FWHM (radians), θ = Bragg angle. Using the principal peak at $2\theta \approx 31.98°$ (FWHM ≈ 0.181°), $D \approx 38.71$ nm was obtained. Overall, crystallite sizes ranged 30–58 nm across major peaks, reflecting enhanced crystallinity and Cobalt-rich phase development [13].

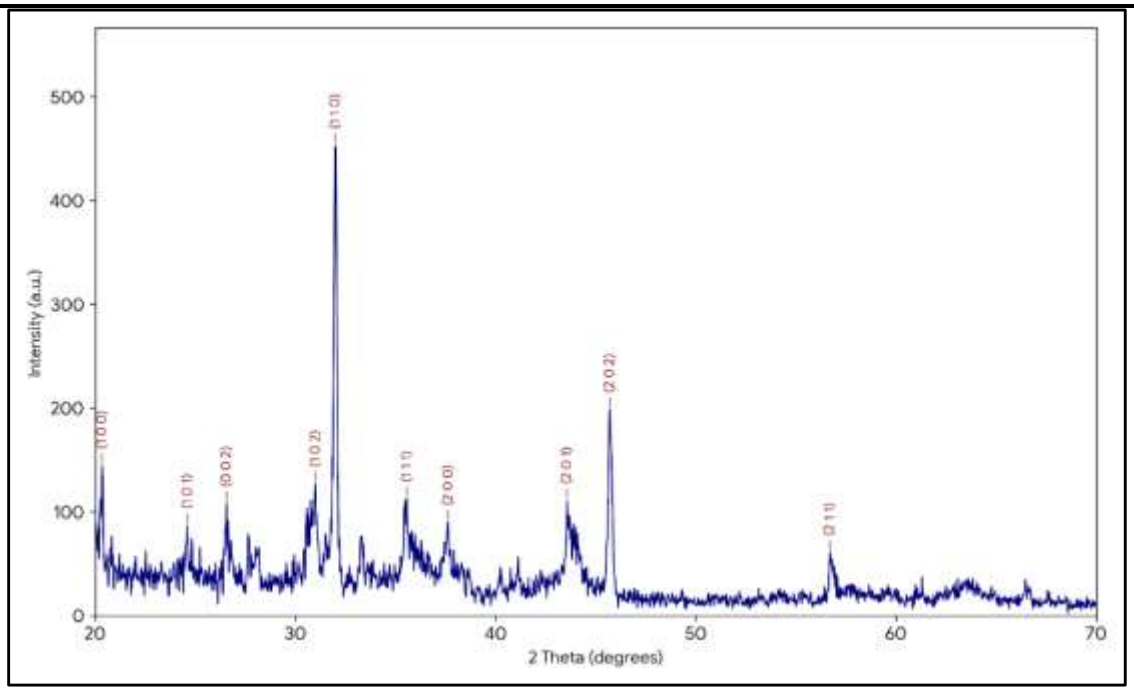

Figure 4: XRD pattern of Co_3NiBaO_6 photocatalyst

Table 1: crystal size of Co_3BaNiO_6 photocatalyst

S. No.	Angle 2θ	d-spacing (Å)	FWHM (°)	Relative Intensity (%)	Crystal size (nm)	Average crystal size (nm)
1.	20.34	4.36	0.179	32	45.2	
2.	24.60	3.62	0.180	19	45.1	
3.	26.56	3.35	0.142	24	57.7	
4.	31.00	2.88	0.350	28	23.5	
5.	**31.98**	**2.80**	**0.181**	**100**	**45.8**	**38.71 nm**
6.	35.56	2.52	0.261	25	32.0	
7.	37.62	2.39	0.202	20	41.7	
8.	43.56	2.08	0.286	24	29.9	
9.	45.70	1.98	0.238	44	36.2	

3.5. Band gap calculation:

The optical properties of the synthesized Co_3NiBaO_6 nanomaterial were investigated using a UV-Vis absorption spectrophotometer (Figure 5). The absorption coefficient (α) was calculated using the relation $\alpha = 2.303\ A/t$, where A is absorbance and t is thickness. The optical bandgap energy (Eg) was determined by extrapolating the linear portion of the Tauc plot $[(\alpha\ h\nu)^2$a.u.vs photon energy (hν),] to the x-axis (Figure 6), following the standard method adopted for similar oxide nanocomposites [14][15]. The spectrum revealed an absorption peak at 495-496 nm. The calculated optical bandgap was found to be ≈3.29 eV. This value is lower than pure NiO, which can be attributed to the successful integration of Co and Ba ions into the lattice, similar to the band gap modulation reported in Mn-doped NiO and other nickel-based oxides [16][17].

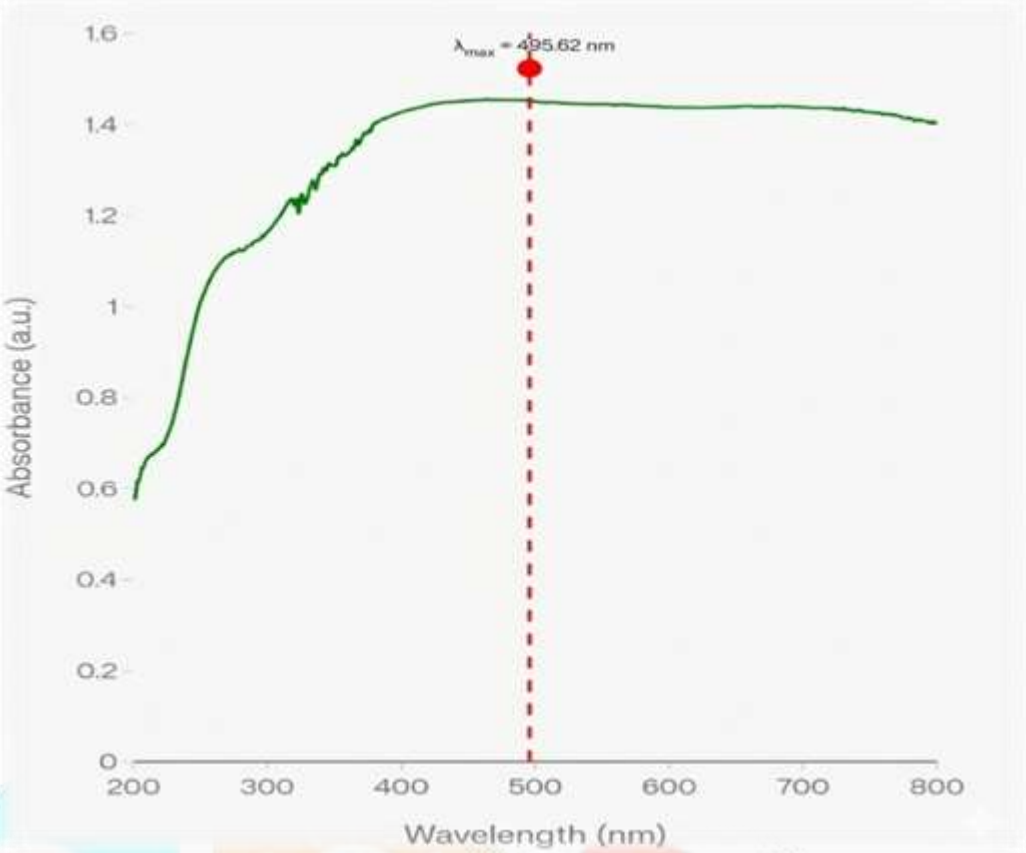

Figure 5: UV-VIS spectra peak absorption

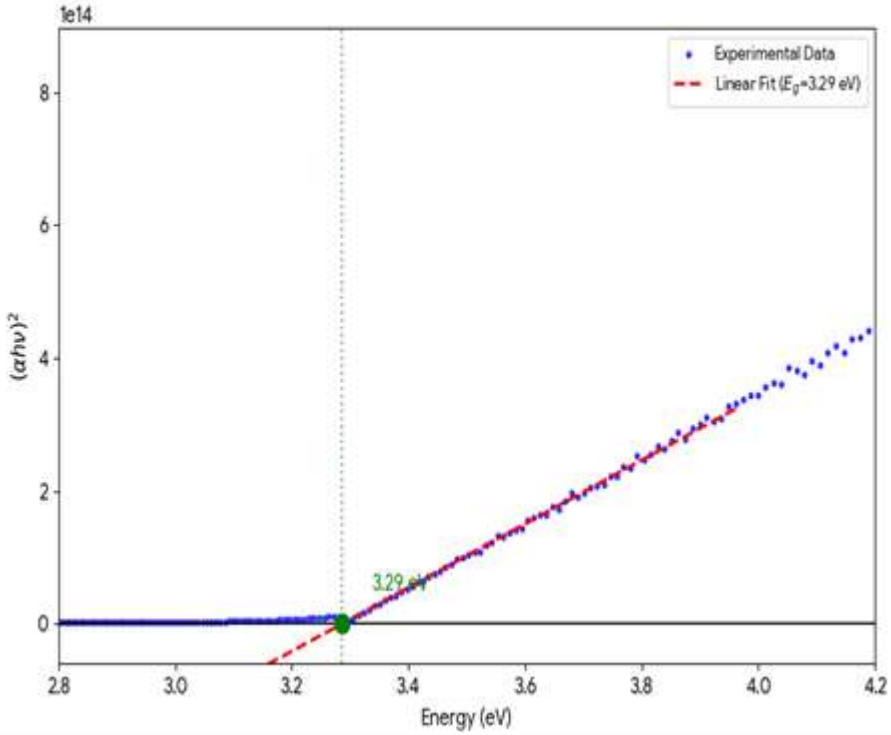

Figure 6: UV-VIS spectra for bandgap

3.6. Photoluminescence (PL) Spectroscopy Analysis

Photoluminescence (PL) spectroscopy (excitation at 290 nm) was employed to investigate the optical properties and electronic transitions of the synthesized Co_3NiBaO_6 catalyst, complementing the UV-Vis absorption results. UV-Vis analysis revealed a wide optical bandgap of 3.29 eV with a strong absorption maximum at 493.62 nm. The PL spectrum (Figure 7) exhibited a high-energy emission peak at 350.4 nm, attributed to intrinsic lattice transitions involving ligand-to-metal charge transfer (LMCT) from O^{2-} to Co/Ni/Ba centres - typical of complex barium-transition metal oxides [18][21][23].

The 412.1 nm (3.01 eV) emission corresponds to near-band-edge (NBE) recombination. The observed Stokes shift—difference between the 3.29 eV (377 nm) bandgap and this peak—arises from photoexcited carrier relaxation into shallow trap states prior to radiative decay, a phenomenon common in Ba-based multimetallic oxides due to Ba^{2+}-induced lattice distortions [19].

Sub-bandgap emissions at 437.4 nm and 465.8 nm indicate oxygen vacancies and surface defects. These act as charge carrier traps in ternary/quaternary oxides, extending carrier lifetimes and boosting catalytic efficiency. The intensity rise near 500 nm aligns with the UV-Vis λ_max of 493.62 nm, verifying Co/Ni d-d crystal field transitions. Overall, this band gap-PL synergy confirms Co_3NiBaO_6 as an electronically active semiconductor ideal for photocatalysis [20-23].

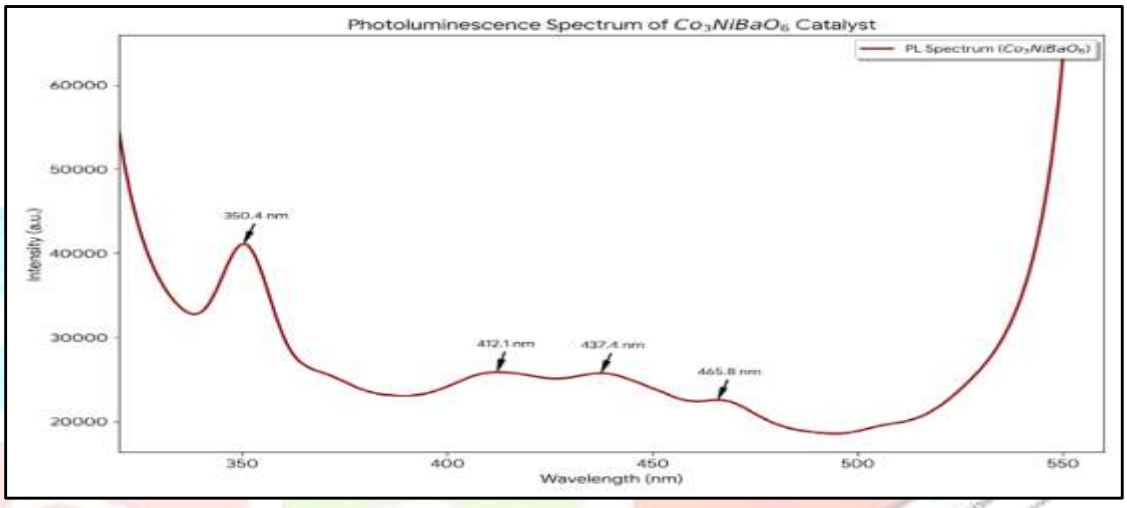

Figure 7 : Photoluminescence Analysis of Co_3NiBaO_6 Nanomaterial

3.7. FTIR analysis

FTIR analysis is carried out in the 400-4000 cm^{-1} frequency range and the resulting spectra is given in figure 8.

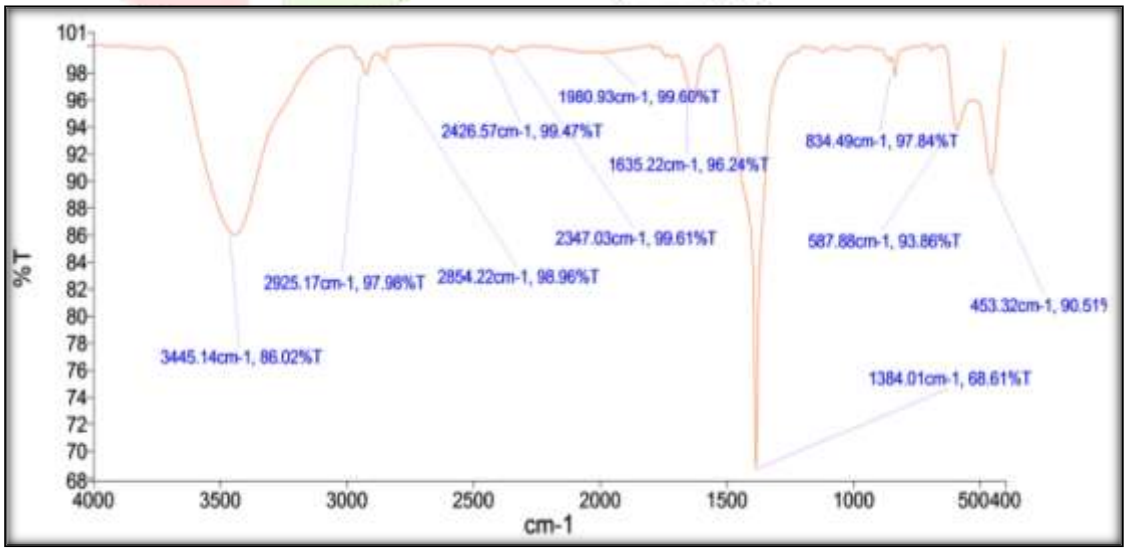

Figure 8: IR spectra of Co_3NiBaO_6 photocatalyst

3.8. Photocatalytic activity of Co_3NiBaO_6 nanoparticles

Figure 9 displayed a linear plot of (1 + log O.D.) versus time. Pseudo-first-order kinetics best fit the degradation data among tested models (pseudo-first/second-order Types 1-5). Optimized TB dye conditions: pH 9.0 0.16g catalyst, 4×10^{-5} M dye, 1640 mW/cm² light. RR 35: pH 4.5, 0.14 g catalyst, 8×10^{-5} M dye, 1440 mW/cm²; EY: pH 4.5, 0.14 g catalyst, 0.75×10^{-5} M dye, 1440 mW/cm². Precise parameter control ensures efficient dye removal. A comparative study of degredation of three dyes are shown in table 2.

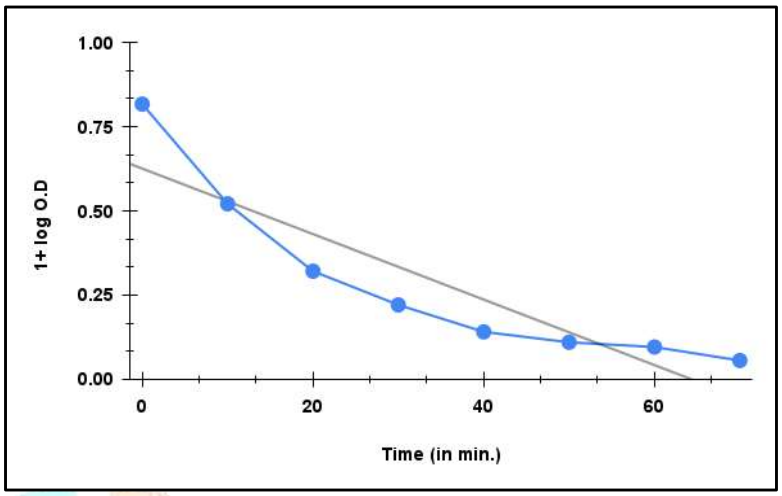

(a)

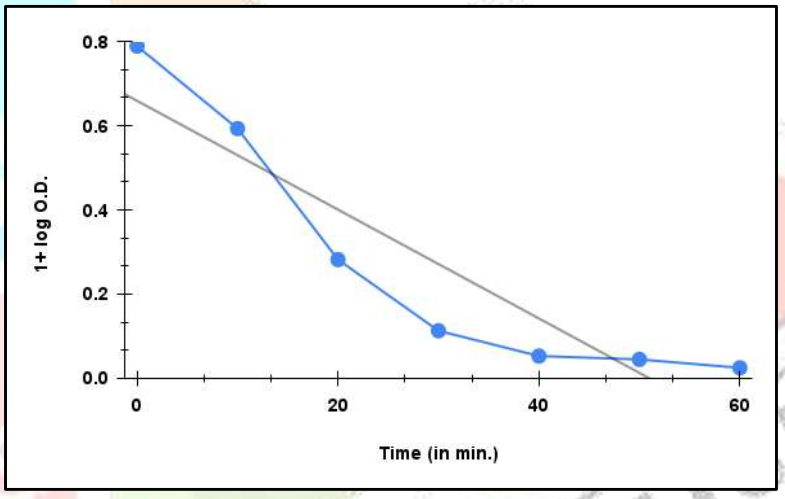

(b)

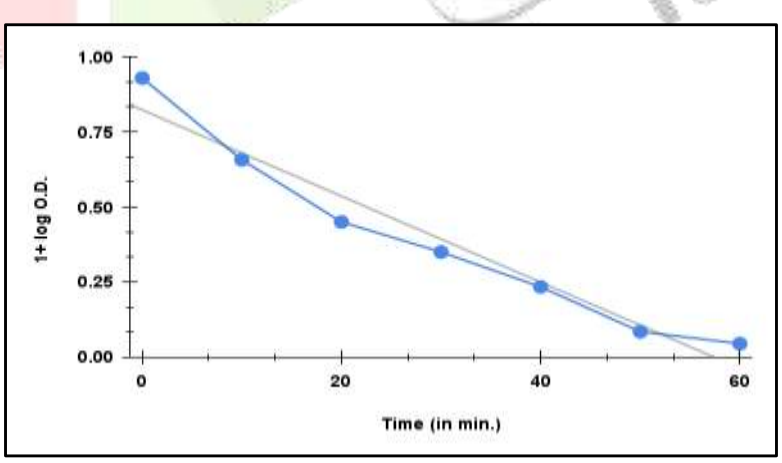

(c)

Figure 9: Photo Catalytic activity of Co_3NiBaO_6 for degradation of (a) Toludine Blue (b) Eosin Yellow (c) Reactive Red-35 A typical run

Table 2 : Comparative study of degradation of three dyes

Name of the group	Name of the dye	Observed Parameters					Removal efficiency (%)
		λ_{max} (nm)	pH	Co_3NiBaO_6 (g)	Dye Concentration (M)	Light intensity mW/cm²	
Thiazine	Toluidine Blue	630	9.0	0.16	4×10^{-5}	1640	80.94 in 70 min
Xanthene	Eosin yellow	520	4.5	0.14	0.75×10^{-5}	1440	82.76 in 40 min
Azo	Reactive Red-35	515	4.5	0.14	8×10^{-5}	1440	88.05in 60 min

3.8.1. Effect of photocatalyst doses:

The effect of photocatalyst dosage on the degradation efficiency was systematically examined by varying the catalyst weight while keeping all other parameters constant. The results, illustrated in figure 10, indicate that maximum degradation occurred at a photocatalyst loading of 0.14 g for Reactive Red and Eosin Yellow, and 0.16 g for Toluidine Blue. This enhancement is attributed to the increased surface area available for light absorption, leading to the generation of a higher number of electron–hole pairs. However, further increasing the catalyst dosage resulted in a decline in reaction rate, likely due to enhanced electron–hole recombination and light scattering at higher particle concentrations.

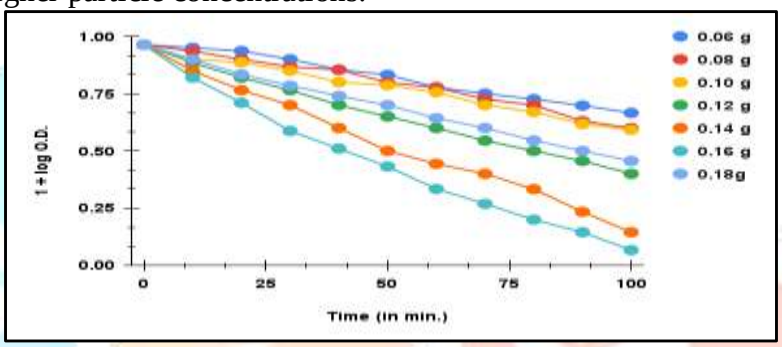

(a)

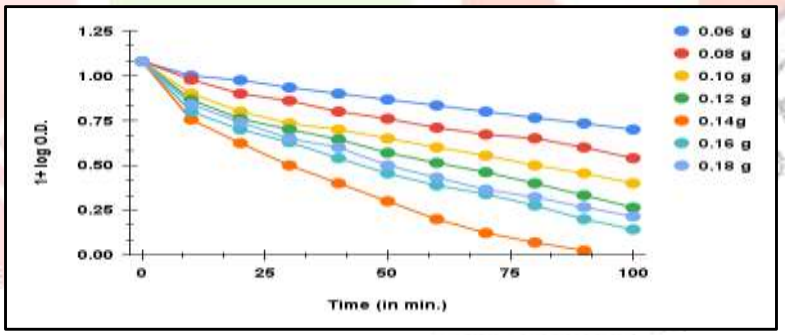

(b)

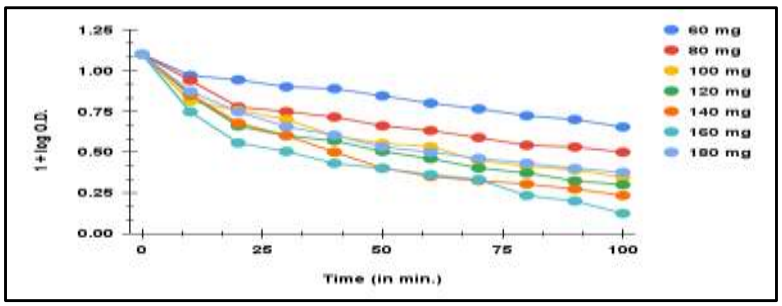

(c)

Figure 10: Photodegradation by Co_3NiBaO_6 at different photocatalyst Dosage in gram
(a) Toludine blue (b) Eosin yellow (c) Reactive red 35

3.8.2 Effect of dye concentration

The influence of initial dye concentration on photocatalytic degradation was investigated while keeping all other parameters constant. The results for Toluidine Blue (TB), Eosin Yellow (EY), and Reactive Red 35 (RR 35) are presented in figure 11. The reaction rate initially increased with rising dye concentration due to the greater availability of dye molecules capable of absorbing photons and becoming photoexcited. However, beyond the optimal concentrations of 4×10^{-5} M for TB, 8×10^{-5} M for RR 35, and 0.75×10^{-5} M for EY, the degradation rate declined. This reduction is attributed to excessive dye molecules darkening the solution, thereby acting as a light filter and hindering photon penetration to the catalyst surface.

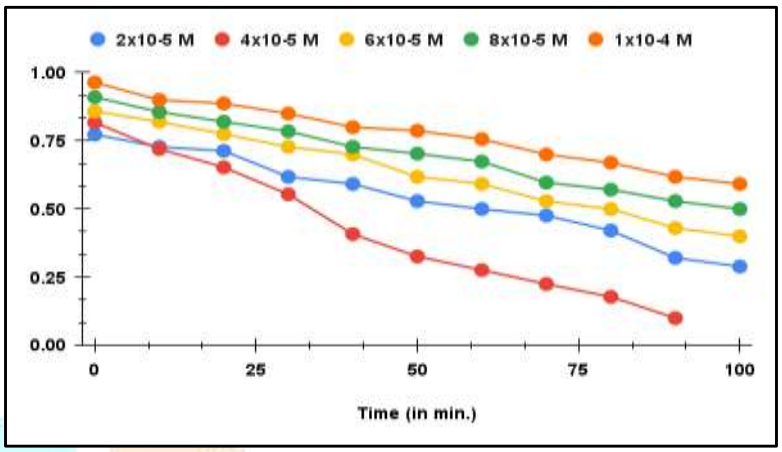

(a)

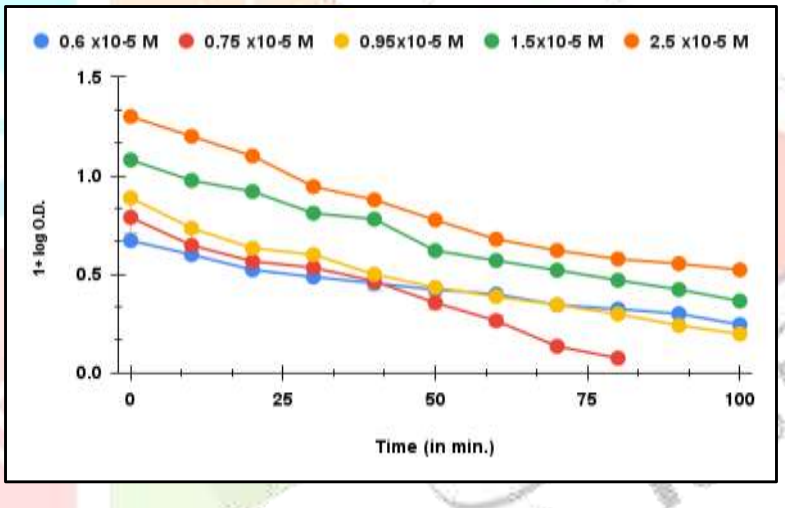

(b)

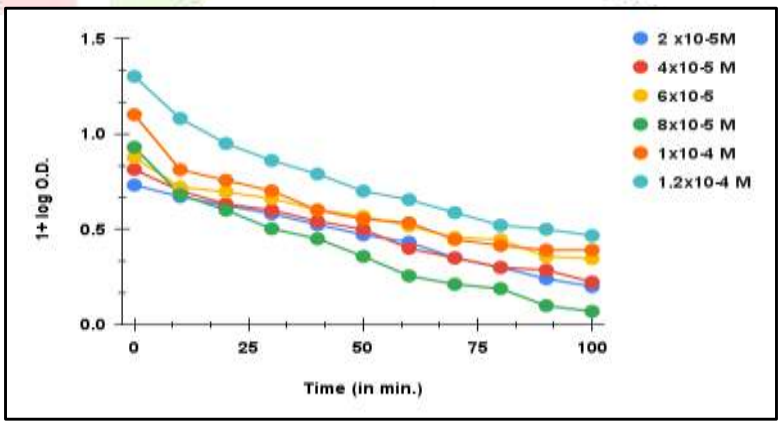

(c)

Figure 11: Photodegradation by Co_3NiBaO_6 at different concentration of (a) Toludine blue (b) Eosin yellow (c) Reactive red 35

3.8.3. Effect of intensity of light:

The effect of light intensity on photocatalytic degradation was investigated within the range of 1090–1800 mW/cm², while maintaining all other parameters constant.The corresponding results are illustrated in Figure 12. An increase in degradation rate was observed with rising light intensity, owing to the higher photon flux striking the catalyst surface, which generates more excited dye molecules and electron–hole pairs. The maximum degradation efficiencies were obtained at 1440 mW/cm² for RR 35 and EY, and at 1640 mW/cm² for TB. Beyond these intensities, the reaction rate declined due to enhanced recombination of photogenerated charge carriers, which reduces the availability of reactive species responsible for dye degradation.

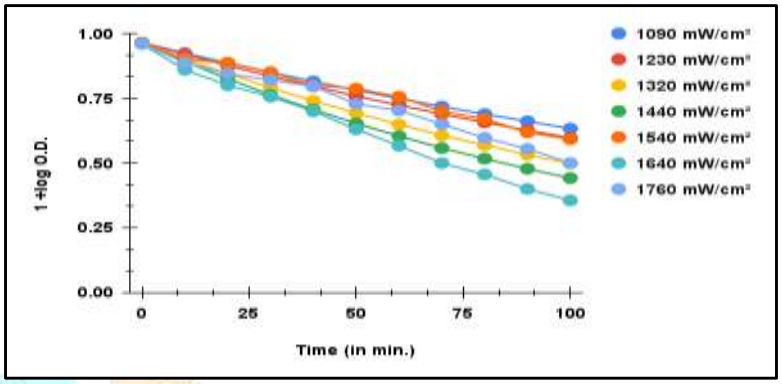

(a)

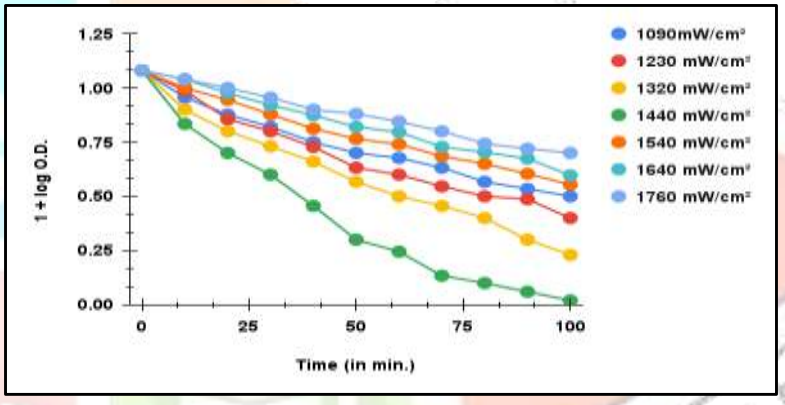

(b)

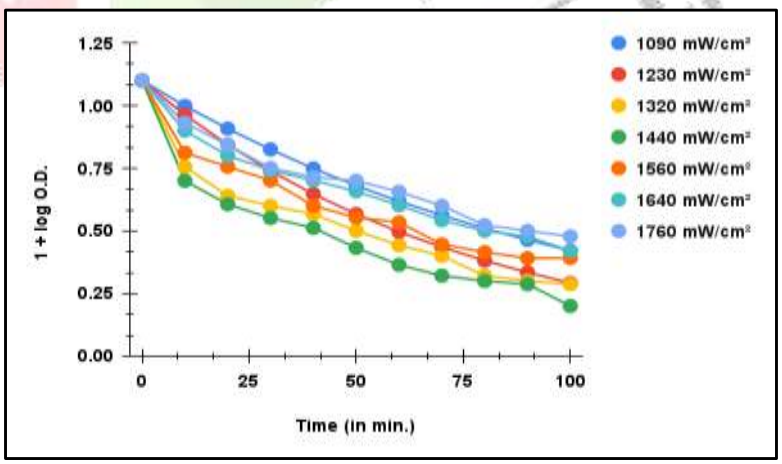

(c)

Figure 12: Photodegradation by Co_3NiBaO_6 at different intensity of light
(a) Toludine blue (b) Eosin yellow (c) Reactive red 35

3.8.4. Effect of pH

The rate of dye degradation was found to vary significantly with the pH of the solution, as dyes are highly sensitive to pH fluctuations—some even exhibit distinct color changes with varying pH. To explore this effect, the solution pH was systematically adjusted between 3 and 10 while keeping all other parameters constant. Corresponding variations in initial optical density were recorded, as illustrated in Figures 13 (a–c) for Toluidine Blue, Reactive Red 35, and Eosin Yellow, respectively. The results demonstrate the critical role of pH in influencing photocatalytic activity. The degradation rate increased with rising pH for Toluidine Blue, reaching an optimum at pH 9.0, whereas Reactive Red 35 and Eosin Yellow showed higher degradation efficiencies under acidic conditions, with maximum rates observed at pH 4.5 for both dyes.

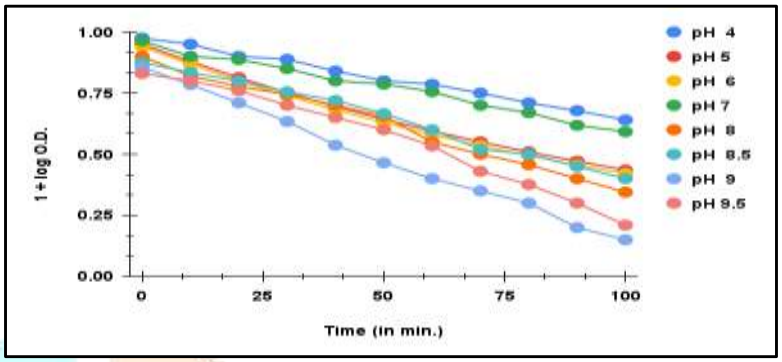

(a)

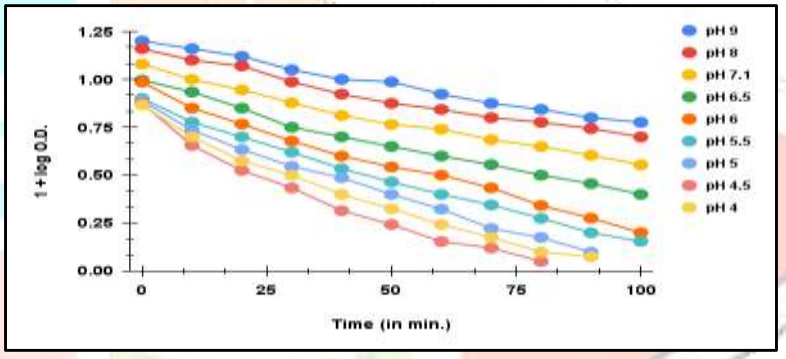

(b)

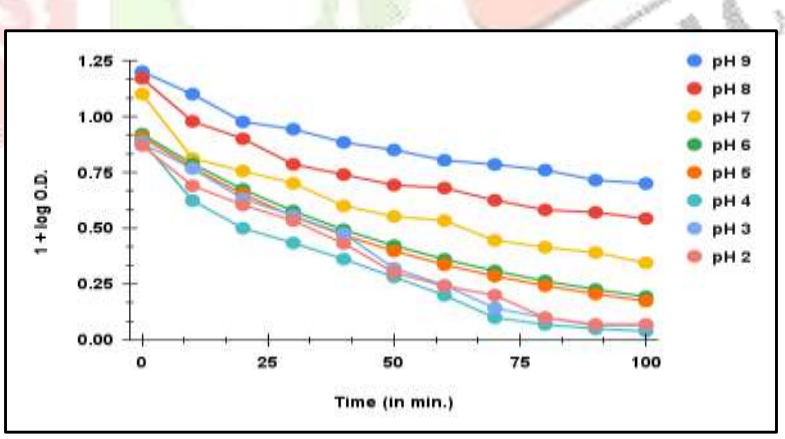

(c)

Figure 13: Photodegradation by Co_3NiBaO_6 at different Ph
(a) Toluidine blue (b) Eosin yellow (c) Reactive red 35

3.8.5. Ascertaining the reactive species:

The experimental findings (Figure 14) clearly indicate that the addition of EDTA to Toluidine Blue, KI to Eosin Yellow, and isopropanol to Reactive Red 35 solutions effectively suppressed photocatalytic degradation. This confirms that photogenerated holes (h^+) play a dominant role in the degradation of Toluidine Blue and Eosin Yellow, while hydroxyl radicals serve as the primary oxidative species for Reactive Red 35. Quantitative results further verify that, under visible-light irradiation, both h^+ and hydroxyl radicals are generated in the photocatalytic system and act as the key reactive intermediates responsible for dye decolorization [24].

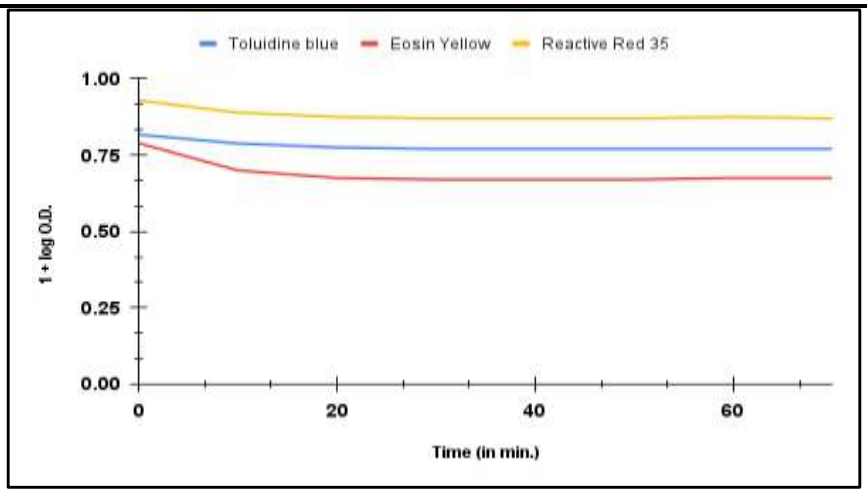

Figure 14: Photodegradation by Co_3NiBaO_6in scavenger

(a) Toludine blue (b) Reactive red-35 (c) Eosin yellow

Elementary Reaction Sequence (Generalized for all examined dyes):

(1) $^1Dye^0$ (TB,EY and RR) $\rightarrow$ $^1Dye^1$ (TB,EY and RR)

(2) $^1Dye^1$ (TB,EY and RR) $\rightarrow$ $^1Dye^3$ (TB,EY and RR)

(3) Catalyst $(e^- + h^+) \rightarrow$ Catalyst $[e^-$ (CB) + h^+ (VB)]

(4) $e^- + O_2 \rightarrow O_2^{\bullet -}$

(5) $h^+ + H_2O \rightarrow OH^\bullet + H^+$

(6) $h^+ + OH^- \rightarrow OH^\bullet$

(7) $AA + O_2^{\bullet -} \rightarrow CO_2 + H_2O + N_2 + NO_2$ etc.

(8) EB & CR + $OH^\bullet \rightarrow CO_2 + H_2O + N_2 + NO_2$ etc.

The last two steps for each individual dye (TB, EY and RR)) depending on which radical ($O_2\bullet^-$ or •OH) scavenger studies identify as the dominant oxidizing species.

3.8.6 Recycling of the photocatalyst

The recovered photocatalyst was recycled i.e. washed and calcined again. This was then used for degradation of all dyes and it was observed that its efficiency remained unaltered even after its repeated use for next four cycles. This property makes it more valuable to be used as potential photocatalyst in environmental remediation.

IV. CONCLUSION

The Co_3NiBaO_6 nanoparticles were successfully synthesized via the co-precipitation method, achieving a yield efficiency of 87.12% after calcination. Comprehensive characterization using XRD, FE-SEM, EDS, XPS, IR, UV–Vis spectroscopy, and PL analysis confirmed the formation of well-crystallized nanoparticles with an average crystallite size of 38.71 nm, exhibiting structural and morphological features favorable for photocatalytic applications. The as-synthesized photocatalyst showed excellent performance in the photodegradation of Toluidine Blue (TB), Reactive Red 35 (RR 35), and Eosin Yellow (EY) dyes under visible light. The degradation efficiency increased with catalyst dosage up to an optimum value, and was further influenced by initial dye concentration, pH, and light intensity, highlighting the system's strong sensitivity to reaction conditions.

V. ACKNOWLEDGMENTS

The authors gratefully acknowledge the University Grants Commission (UGC) for providing financial assistance through fellowship support. Sincere thanks are also extended to the Materials Research Centre (MRC), MNIT Jaipur, for offering advanced research facilities. The authors highly appreciate the MRC team's assistance with data analysis and characterization.

REFERENCE

1. Khan, S., Noor, T., Iqbal, N., Yaqoob, L. 2024. Photocatalytic dye degradation from textile wastewater: a review. ACS Omega, 9(20): 21751-21767.
2. Irshad, M., tul Ain, Q., Zaman, M., Aslam, M. Z., Kousar, N., Asim, M., Imran, M. 2022. Photocatalysis and perovskite oxide-based materials: a remedy for a clean and sustainable future. RSC Advances, 12(12): 7009-7039.
3. Saravan, R. S., Muthukumaran, M., Mubashera, S. M., Abinaya, M., Prasath, P. V., Parthiban, R., Sagadevan, S. 2020. Evaluation of the photocatalytic efficiency of cobalt oxide nanoparticles towards the degradation of crystal violet and methylene violet dyes. Optik, 207: 164428.
4. Nandiyanto, A. B. D., Ragadhita, R., Anggiat, L. S. 2024. Synthesis of barium oxide nanoparticles: Optical properties and application in degradation indigotine dye. Moroccan Journal of Chemistry, 12(2): 627-642.
5. Ramesh, P., Rajendran, A. 2022. Green synthesis of nickel oxide nanoparticles for photodegradation analysis. Materials Today: Proceedings, 68: 367-372.
6. Biesinger, M. C., Payne, B. P., Grosvenor, A. P., Lau, L. W., Gerson, A. R., Smart, R. S. C. 2011. Resolving surface chemical states in XPS analysis of first row transition metals, oxides and hydroxides: Cr, Mn, Fe, Co and Ni. Applied Surface Science, 257(7): 2717-2730.
7. Singh, V., Major, D. T. 2016. Electronic structure and bonding in Co-based single and mixed valence oxides: A quantum chemical perspective. Inorganic Chemistry, 55(7): 3307-3315.
8. Verhoeven, J. T., Van Doveren, H. 1980. XPS studies on Ba, BaO and the oxidation of Ba. Applications of Surface Science, 5(4): 361-373.
9. Idriss, H. 2021. On the wrong assignment of the XPS O1s signal at 531–532 eV attributed to oxygen vacancies in photo-and electro-catalysts for water splitting and other materials applications. Surface Science, 712: 121894.
10. Takeda, Y. 1975. Magnetic property in the system $BaCo_{1-x}Ni_xO_3$ (x= 0∼ 1). Journal of Solid State Chemistry, 15(1): 40-44.
11. Lee, J. G., Hwang, J., Hwang, H. J., Jeon, O. S., Jang, J., Kwon, O., Shul, Y. G. 2016. A new family of perovskite catalysts for oxygen-evolution reaction in alkaline media: $BaNiO_3$ and $BaNi_{0.83}O_{2.5}$. Journal of the American Chemical Society, 138(10): 3541-3547.
12. Felser, C., Yamaura, K., Cava, R. J. 1999. The electronic structure of hexagonal $BaCoO_3$. Journal of Solid State Chemistry, 146(2): 411-417.
13. Monshi, A., Foroughi, M. R., Monshi, M. R. 2012. Modified Scherrer equation to estimate more accurately nano-crystallite size using XRD. World Journal of Nano Science and Engineering, 2(3): 154-160.
14. Amjad, M., Bibi, I., Majid, F., Jilani, K., Sultan, M., Raza, Q., Iqbal, M. 2024. $NiO/MnFe_2O_4$ nanocomposite photoluminescence, structural, morphological, magnetic, and optical properties: photocatalytic removal of cresol red under visible light irradiation. ACS Omega, 9(19): 20876-20890.
15. Islam, R., Abdur, R., Alam, M. A., Munna, N., Ahmed, A. N., Hossain, M., Jamal, M. S. 2025. Modulating Mn-doped NiO nanoparticles: structural, optical, and electrical property tailoring for enhanced hole transport layers. Nanoscale Advances, 7(1): 133-143.
16. Suram, S. K., Zhou, L., Shinde, A., Yan, Q., Yu, J., Umehara, M., Gregoire, J. M. 2018. Alkaline-stable nickel manganese oxides with ideal band gap for solar fuel photoanodes. Chemical Communications, 54(36): 4625-4628.
17. Parimon, N., Mamat, M. H., Banu, I. S., Vasimalai, N., Ahmad, M. K., Suriani, A. B., Rusop, M. 2021. Annealing temperature dependency of structural, optical and electrical characteristics of manganese-doped nickel oxide nanosheet array films for humidity sensing applications. Nanomaterials and Nanotechnology, 11: 1847980420982788.
18. Peng, H., et al. 2020. Origin of the Photoluminescence of Metal Nano-clusters. Small, 16(9): 1907686.
19. Park, C. H., et al. 2004. Strong Near-Infrared Luminescence in $BaSnO_3$. Journal of the American Chemical Society, 126(41): 13126-13127.
20. Huang, H., et al. 2024. Plasma-Induced Oxygen Defect Engineering in Perovskite Oxides for Enhanced OER. Advanced Functional Materials, DOI: 10.1002/adfm.202413456.
21. Craddock, E. P., et al. 2025. Local coordination geometry within cobalt spinel oxides governs optical and electronic properties. Chem. Sci., DOI: 10.1039/D5SC01909E.
22. Gupta, S., et al. 2023. Recent progress in defect-engineered metal oxides for photocatalytic environmental remediation. Photochemistry and photobiology, DOI: 10.1111/php.13959.
23. Huang, W. 2020. Transition metal–based composites for oxygen evolution reaction. PhD Thesis,

Technical University of Denmark.
24. Anonymous. 2020. A critical view about use of scavengers for reactive species in heterogeneous photocatalysis. Microchemical Journal, 157: 105013.